

Revisiting the Architecture of the KOI-89 System

KENTO MASUDA ¹ AND DANIEL TAMAYO ^{2,*}

¹*Department of Earth and Space Science, Osaka University, Osaka 560-0043, Japan*

²*Department of Astrophysical Sciences, Princeton University, Princeton, NJ 08544, USA*

(Received July 28, 2020; Revised September 11, 2020; Accepted September 14, 2020)

ABSTRACT

While high stellar obliquities observed in exoplanetary systems may be attributed to processes that tilt the planetary orbits, it is also possible that they reflect misalignments between protoplanetary disks and stellar spins. This latter hypothesis predicts the presence of co-planar multi-planetary systems misaligned with their central stars. Here we re-evaluate the evidence of such an architecture that has been claimed for the KOI-89 system. KOI-89 is an early-type star with one validated transiting planet KOI-89.01/Kepler-462b (period 84.7 days, radius $3.0 R_{\oplus}$) and one transiting planet candidate KOI-89.02 (period 207.6 days, radius $4.0 R_{\oplus}$), where the latter exhibits transit timing variations (TTVs). A previous modeling of the stellar gravity-darkening effect in the transit light curves inferred a high stellar obliquity of $\approx 70^\circ$. We perform a photodynamical modeling of the *Kepler* transit light curves, and use the resulting constraints on the orbital configuration and transit times to update the gravity-darkened transit model. As a result, we find no firm evidence for gravity darkening effect in the transit shapes and conclude that stellar obliquity is not constrained by the data. Given evidence for low orbital eccentricities from the dynamical analysis, the system architecture can thus be consistent with many other multi-transiting systems with flat, near-circular orbits aligned with the stellar spin. We find that the TTVs imparted on its neighbor imply that KOI-89.01 has a mass $\gtrsim 20 M_{\oplus}$. This would render it one of the densest known sub-Neptunes, mostly composed of a solid core. Lower masses are possible if the TTVs are instead due to an unseen third planet.

1. INTRODUCTION

The approximate alignment between the Sun’s rotation and the orbital motion of our Solar System’s planets appears to be a natural consequence of planet formation in a protoplanetary disk. Yet, measurements of stellar obliquities in transiting exoplanetary systems have revealed that this is not always the case. Stellar obliquities have been constrained in more than 100 systems¹, and large stellar obliquities have been reported not only for hot Jupiters (e.g., Hébrard et al. 2008) but also for planets smaller than about Neptune (e.g., Winn et al. 2010b; Bourrier et al. 2018; Kamiaka et al. 2019; Kuno-vac Hodžić et al. 2020)

It remains an open question whether the planets are to blame or not for those misalignments. They may orig-

inate from post-formation perturbations due to planet-planet scattering (Rasio & Ford 1996; Weidenschilling & Marzari 1996; Chatterjee et al. 2008; Jurić & Tremaine 2008) or secular interactions with a stellar/planetary companion (Mazeh et al. 1997; Holman et al. 1997; Fabrycky & Tremaine 2007; Naoz et al. 2011). If this is the case, stellar obliquities would serve as a probe of dynamical evolution of planetary orbits.

Alternatively, high stellar obliquities may simply reflect primordial misalignments between stellar equators and their surrounding protoplanetary disks: disks may be born misaligned with their host stars due to chaotic accretion of angular momentum expected from a turbulent molecular cloud (Bate et al. 2010; Fielding et al. 2015; Takaishi et al. 2020), or disks may be tilted after the formation due to (combined effects of) torques from an exterior stellar companion and gravitational/magnetic star–disk interactions (Batygin 2012; Batygin & Adams 2013; Spalding & Batygin 2014; Lai 2014; Spalding & Batygin 2015; Zanazzi & Lai 2018). Alternatively, a massive star’s surface rotation might be reoriented after disk/planet formation due to angular

Corresponding author: Kento Masuda
kmasuda@ess.sci.osaka-u.ac.jp

* NASA Sagan Fellow

¹ A summary can be found in TEPCAT (<https://www.astro.keele.ac.uk/jkt/tepcat/tepcat.html>; Southworth 2011).

momentum transport via internal gravity waves (Rogers et al. 2012).

To test this latter possibility, two complementary methods have been pursued. First, one can search for misalignments between stars and their protoplanetary disks. Because stars fully embedded in their protoplanetary disks cannot be observed, such measurements have been performed for resolved debris disks as proxies of the original protoplanetary disks (Watson et al. 2011; Greaves et al. 2014), and for protoplanetary disks in the late phase of evolution (Davies 2019). While the majority of these disks appear to be star-aligned (Watson et al. 2011; Greaves et al. 2014), some candidates for misaligned systems have also been presented (Davies 2019). A possibly confounding factor is that the inner disk regions more relevant to the observed exoplanet population could be aligned, even though the resolved outer regions are misaligned.

The second possibility, which we focus on in this paper, is to use nearly coplanar multi-planet systems, whose orbits appear to have remained intact after formation. Obliquities have been measured for a dozen of stars with multiple transiting planets to date (Sanchis-Ojeda et al. 2012; Hirano et al. 2012; Albrecht et al. 2013; Chaplin et al. 2013; Huber et al. 2013; Sanchis-Ojeda et al. 2015; Ahlers et al. 2015; Wang et al. 2018; Zhou et al. 2018; Dalal et al. 2019; Hirano et al. 2020; Mann et al. 2020). These multi-transiting systems most likely (though not always; Mills & Fabrycky 2017) have aligned orbital planes that trace the initial protoplanetary disk.

While most of these measurements are consistent with low ($\lesssim 10^\circ$) stellar obliquity, three of these systems, Kepler-56 (Huber et al. 2013), KOI-89 (Ahlers et al. 2015), and HD 3167 (Dalal et al. 2019) have strong claimed misalignments. If the planets in these systems trace their natal disk, they are smoking guns for an obliquity excitation process independent of orbital evolution.

However, the Kepler-56 planets may not trace the original plane of the protoplanetary disk. There is in fact a third massive ($\gtrsim 5.5 M_{\text{Jup}}$) planet on an au-scale, eccentric orbit (Otor et al. 2016) exterior to the two transiting planets. Follow-up studies have shown that gravitational interactions with the outer planet could have tilted the inner orbits out of alignment with the host star while preserving their mutual coplanarity, owing to the tight gravitational coupling between the inner transiting planets (Li et al. 2014; Lai & Pu 2017; Gratia & Fabrycky 2017; Huang et al. 2017). Dalal et al. (2019) argued that the same could well be the case for HD 3167 too: they reported a possible signature of an

outer companion in the radial velocity data, and showed that the hypothetical companion is physically capable of generating a high stellar obliquity while maintaining the co-planarity of the inner system.²

That leaves KOI-89 as the best candidate for misalignments unrelated to orbital evolution, including primordial star-disk misalignment. Even if undetected companions existed in the system, the transiting planets are more widely separated than in the above systems and are thus less likely to maintain co-planarity under plausible external perturbations. In this light, it is particularly important to evaluate the evidence for the claimed high obliquity of KOI-89, and/or to search for potential signature of mutual orbital misalignment.

The high ($\approx 70^\circ$) stellar obliquity of KOI-89 was inferred (Ahlers et al. 2015) by modeling the gravity-darkening effect (von Zeipel 1924) in transit light curves (Barnes 2009). However, the solution involved a large ($\gtrsim 0.5$) orbital eccentricity for KOI-89.02 that may make its orbit cross with the inner one, suggesting that there is something missing in the modeling. A wrong inference for the eccentricity could also bias the transit impact parameters and hence the obliquity measurement. In addition, KOI-89.02 exhibits strong transit timing variations (TTVs) that can further complicate the analysis of the transit shape.

In this paper, we revisit the geometric architecture of the KOI-89 system, in particular the constraint on stellar obliquity, by fully exploiting the information from transit shapes and TTVs. In Section 2, we characterize the host star combining archival photometry, spectroscopy, and astrometry data. Given the large number of additional parameters required to model transits across a potentially tilted, gravity-darkened star, we begin with a photodynamical analysis ignoring the effect of rapid stellar rotation (Section 3). We then fold in the resulting constraints on the orbital configuration to evaluate the evidence for a non-zero stellar obliquity in Section 4. From these analyses, we find that the stellar obliquity is not well constrained and that the architecture of the system can in fact be consistent with a flat, near-circular geometry as inferred for most other multi-transiting systems. Section 5 puts this updated measurement into context, and discusses the potentially interesting physical nature of the planets inferred from our photodynamical modeling.

² Although these explanations require that the outer giant has a misaligned orbit relative to the inner planets, there has been accumulating observational evidence that such misaligned systems exist (Masuda et al. 2020; Xuan & Wyatt 2020; De Rosa et al. 2020; Damasso et al. 2020).

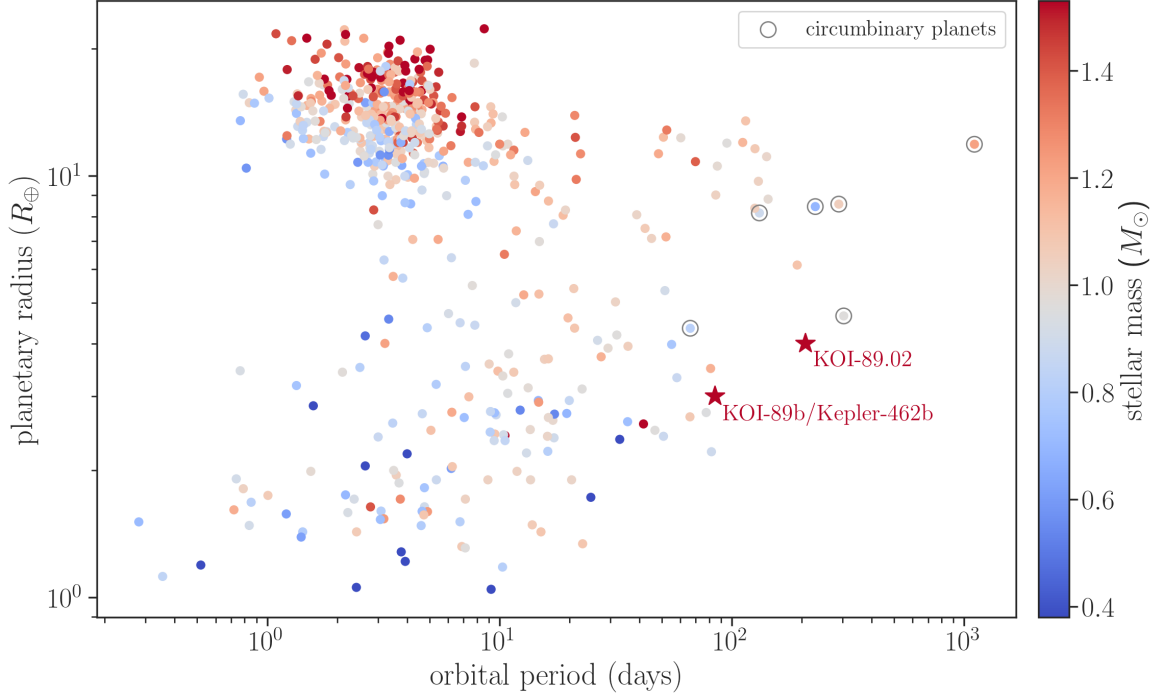


Figure 1. KOI-89 planets are among the longest-period, smallest transiting planets with mass constraints, especially around single host stars more massive than the sun. The colored circles are radii and orbital periods of planets with mass constraints from the NASA exoplanet archive, where planets without reported uncertainties and those from direct imaging observations are not shown. Planets orbiting two stars are marked with outer gray circles.

2. STELLAR PARAMETERS

We characterized the host star KOI-89 by comparing stellar evolutionary models (Dotter 2016; Choi et al. 2016) computed with Modules for Experiments in Stellar Astrophysics (MESA; Paxton et al. 2011, 2013, 2015) to the atmospheric parameters from spectroscopy, the apparent K -band magnitude, and the distance from *Gaia* Data Release 2 (Gaia Collaboration et al. 2018). We used the *isochrones* package by Morton (2015) to obtain posterior samples for the stellar parameters. The same procedure was adopted in Dai et al. (2018) and was validated using a sample of stars characterized with asteroseismology. The results are summarized in Table 1. The host star KOI-89 is an early-type main-sequence star.

The atmospheric parameters were adopted from the analysis of Large Sky Area Multi-Object Fiber Spectroscopic Telescope (LAMOST; Cui et al. 2012; Luo et al. 2015) spectra by Frasca et al. (2016): $T_{\text{eff}} = 7580 \pm 300$ K, $\log g = 3.88 \pm 0.3$, $[\text{Fe}/\text{H}] = 0.13 \pm 0.2$, where the uncertainties are based on the externally estimated accuracies of the pipeline (Frasca et al. 2016). The K -magnitudes were taken from the Two Micron All Sky Survey (2MASS; Skrutskie et al. 2006). We used the dust map and extinction vector from *Bayestar17* (Green et al. 2018) to correct for extinction in the K -

band, assuming a 30% fractional uncertainty (Fulton & Petigura 2018). The distance is based on Bailer-Jones et al. (2018) rather than the inverse of the parallax.

The derived mass and radius are consistent with those in the version 8 of the *TESS* Input Catalog (TIC; Stassun et al. 2019): $M_{\star} = 1.8 \pm 0.3 M_{\odot}$ and $R_{\star} = 1.62 \pm 0.06 R_{\odot}$. On the other hand, our radius (as well as that in TIC) is slightly smaller than $1.74^{+0.08}_{-0.06} R_{\odot}$ by Berger et al. (2018), essentially because they adopted a lower effective temperature than we did ($T_{\text{eff}} = 6688 \pm 134$ K, $\log g = 4.059 \pm 0.150$, $[\text{Fe}/\text{H}] = -0.210 \pm 0.150$), which originates from the *Kepler* Input Catalog DR 25 (Mathur et al. 2017). The value was originally derived in Rowe et al. (2014) using the *specmatch* algorithm on the Keck HIRES spectrum (Petigura et al. 2013). However, this lower temperature is not supported by the empirical color–temperature relation from Boyajian et al. (2013), which gives $T_{\text{eff}} \approx 7000$ K for $V - J$, $V - H$, $V - K$ even without correcting for extinction; the true color of the star should be bluer, and so the true temperature should be higher. We also reduced the archival Keck HIRES spectrum³ using the CERES pipeline (Brahm et al. 2017a) and derived stellar atmo-

³ Downloaded from the Keck observatory archive. <https://koa.ipac.caltech.edu/cgi-bin/KOA/nph-KOAlugin>

Table 1. Parameters of the Host Star KOI-89/Kepler-462.

Parameter	Value
effective temperature (K)	7500 ± 300
log surface gravity (cgs)	4.22 ± 0.04
metallicity (dex)	0.05 ± 0.11
distance (pc)	598 ± 11
mass M_* (M_\odot)	1.59 ± 0.08
radius R_* (R_\odot)	1.62 ± 0.04
mean density ρ_* (g cm^{-3})	0.53 ± 0.06
\log_{10} age (yr)	8.7 ± 0.4
projected rotation velocity $v \sin i_*$ (km s^{-1})	80 ± 3
2MASS K_s -magnitude	10.85 ± 0.02

spheric parameters applying the ZASPE (Brahm et al. 2017b) code, in which we extended the default temperature range using a synthetic spectrum library based on the PHOENIX model atmospheres (Husser et al. 2013). We found $T_{\text{eff}} = 7200 \pm 340$ K, $[\text{Fe}/\text{H}] = -0.04 \pm 0.18$, and $v \sin i = 80 \pm 3$ km/s when we imposed the constraint $\log g = 4.14 \pm 0.1$ which is in between the values from Rowe et al. (2014) and Frasca et al. (2016), and is also consistent with the TIC value. Thus we conclude that $T_{\text{eff}} \approx 7500$ K we adopted is reasonable. The cause of the discrepancy in the Rowe et al. (2014) measurement using the same Keck spectrum remains unclear, but this might be because specmatch was not designed for early-type, rapidly rotating stars.

3. PHOTODYNAMICAL MODELING

Here we model the *Kepler* transit light curves of KOI-89.01/Kepler-462b and KOI-89.02 taking into account their gravitational interactions, and constrain their masses, radii, orbital eccentricities, and orbital inclinations. The analysis establishes the planetary status of KOI-89.02, and shows that the orbits of the two planets are nearly circular and well-aligned. We also check how much the results can change if the TTVs of KOI-89.02 are caused by an outer, undetected planet. Because the analysis here essentially focuses on transit times and durations, we ignore the stellar oblateness and gravity darkening assuming that their effects on the relevant parameters are minor. We will check the consistency of this assumption later in Section 4.

3.1. The Data and Detrending

We analyzed the long-cadence, Pre-search Data Conditioning (PDC) light curves downloaded from the

Mikulski Archive for Space Telescopes.⁴ The transits of each planet were fitted iteratively as described in Masuda (2015), using the analytic light curve model for the quadratic limb-darkening law (Mandel & Agol 2002) as implemented in *batman* (Kreidberg 2015), multiplied by a quadratic polynomial function of time that accounts for longer-term trends. We fit both transit times and mid-durations letting impact parameters to vary for each transit, and the fitted transit times were used to stack transits without binning; then the stacked transits were fitted to update transit-shape parameters for the next iteration. After 10 iterations, the light curve around each transit was divided by the best-fit polynomial. We use these normalized and detrended transit light curves for photodynamical modeling. An overlapping transit around $\text{BJD}_{\text{TDB}} = 2454833 + 912.7$ was omitted from this analysis, but was later used for a consistency check.

3.2. The Model

We fit osculating Jacobi elements defined at $\text{BJD}_{\text{TDB}} = 2454833 + 149$ and mass ratios for each planet, as well as quadratic limb-darkening coefficients (as parameterized in Kipping 2013) and mean density of the star.⁵ We used *TTVFast* (Deck et al. 2014) to compute model mid-transit time, sky-plane velocity, and impact parameter during each transit of each planet. They were used to calculate planet locations on the stellar surface assuming a linear function of time,⁶ and the locations, along with planet-to-star radius ratios and limb-darkening coefficients, were used to calculate the relative flux losses. We again adopted the Mandel & Agol (2002) model for a quadratically limb-darkened star, as implemented in *batman* (Kreidberg 2015), and computed the long-cadence fluxes \mathbf{m} with a supersampling factor of 11. The residuals between the data \mathbf{f} and the transit model \mathbf{m} were modeled as a Gaussian process whose covariance matrix consists of a Matérn-3/2 covariance and a white-noise term. Thus the log-likelihood of the model $\ln \mathcal{L}$ is

$$\ln \mathcal{L} = -\frac{1}{2}(\mathbf{f} - \mathbf{m})^T K^{-1}(\mathbf{f} - \mathbf{m}) - \frac{1}{2} \ln \det K + \text{const.}, \quad (1)$$

⁴ <https://archive.stsci.edu>

⁵ Because the light-curve model alone does not constrain masses and lengths separately, we fix the stellar mass to be $1 M_\odot$ and fit only the density of the star as well as ratios of masses and radii of the star and planets without loss of generality.

⁶ Ignoring the change in the sky-projected velocity during transits has a negligible effect for such long-period planets.

where

$$K_{ij} = (\sigma_i^2 + \sigma_{\text{jit}}^2) \delta_{ij} + \alpha^2 \left(1 + \frac{|t_i - t_j|}{3\rho} \right) \exp \left(-\frac{|t_i - t_j|}{3\rho} \right). \quad (2)$$

Here t_i and σ_i are the time and PDC flux error of the i th data point, respectively. This likelihood was evaluated using `celerite` (Foreman-Mackey et al. 2017).

We assumed a Gaussian prior for the mean stellar density with a central value of 0.53 g cm^{-3} and a width of 0.06 g cm^{-3} based on the results in Section 2. For the other parameters, we adopted uniform or log-uniform priors on the parameters as specified in Table 2. The posterior samples were obtained using the nested-sampling algorithm `MultiNest` (Feroz & Hobson 2008; Feroz et al. 2009, 2013) and its python interface `PyMultiNest` (Buchner et al. 2014). We typically used 4000 live points and a sampling efficiency of 0.8, and kept updating the live points until an evidence tolerance of 0.5 is achieved. We allowed for the detection of multiple posterior modes.

3.3. Results: Two-planet Model

As the simplest possible explanation, we first adopt a two-planet model. We first fit the data assuming log-uniform priors for the planet-to-star mass ratios m_1/M_\star and m_2/M_\star , and a truncated uniform prior $e_1 < 0.8$ and $e_2 < 0.45$ for the orbital eccentricities, where the subscripts 1 and 2 denote KOI-89.01 and KOI-89.02, respectively. These prior limits on e_1 and e_2 ensure that the orbits of the two planets do not cross, i.e., the periastron distance of the outer orbit is larger than the apastron distance of the inner orbit. Crossing orbital configurations lead to rapid instabilities and are thus short-lived.

Figures 2 and 3 compare the posterior models with the data for KOI-89.01 and KOI-89.02, respectively. The constraints on the parameters are summarized in Table 2. Here the mass and radius ratios and stellar density derived from the dynamical modeling were converted into physical masses and radii by sampling the stellar mass from a Gaussian with the central value $1.59 M_\odot$ and width $0.08 M_\odot$ (Section 2). In Figure 4, mid-transit times and durations computed for posterior samples of the model parameters are compared with the values measured by fitting individual transits (see Section A.2). This comparison is to illustrate that the variations in transit times and durations are well captured in our photodynamical modeling, in which we model the whole transit light curves as shown in Figures 2 and 3. We note that the transit times and durations derived by fitting the simultaneous transits of the two planets (shown as diamonds in this figure), which were not included in the

photodynamical modeling, are in reasonable agreement with the posterior predictions conditioned on the other transits. This serves as a sanity check of the modeling.

We checked for long-term stability of our solution by integrating orbital configurations randomly drawn from our posterior samples. The integrations were performed using the IAS15 integrator (Rein & Spiegel 2015) as implemented in the `REBOUND` package (Rein & Liu 2012). The stepsize is automatically controlled to maintain numerical errors near machine precision. All the solutions turned out to be dynamically stable at least for 10^7 inner orbits (i.e., 2.3 Myr) and no sign of instability was found.

From this analysis, we found lower and upper limits on the masses of KOI-89.01 and KOI-89.02, respectively. The former comes from strong TTVs of KOI-89.02 (see top-right panel of Figure 4), and the latter is due to the weak, if any, TTVs of KOI-89.01 (top-left panel of Figure 4). The orbital eccentricities are constrained to be low, mainly by the TTV signals and partly by a combination of the transit shape and prior constraint on the mean stellar density.

The orbital misalignment in the sky plane (Ω_1 in Table 2, approximately equivalent to the mutual inclination given that both planets transit) is found to be small from the lack of significant transit duration variations (TDVs), which would otherwise be induced through the nodal orbital precession caused by the planets' mutual gravitational interactions (Miralda-Escudé 2002). We note that the high (~ 0.9) impact parameter of KOI-89.02 makes its transit duration particularly sensitive to the perturbations perpendicular to its orbit, and that a weak variation is apparent in Figure 4 even for our solution with a small mutual inclination. See Appendix B for more detailed discussion on this mutual inclination constraint.

The weak constraints on mass ratios from this analysis hint that the result can be sensitive to the adopted prior. Thus, we repeated the analysis with uniform priors on mass ratios whose ranges were selected to be $[0, 200] M_\oplus/M_\odot$ and $[0, 50] M_\oplus/M_\odot$ for KOI-89.01 and KOI-89.02 respectively, based on the above result and the radii ($\approx 3 R_\oplus$) of the planets. The range of Ω_1 was also narrowed down to $[-30^\circ, 30^\circ]$ to speed up the convergence. The results are summarized in the right part of Table 2. As expected, the marginal posteriors for the mass ratios changed slightly, although we again recover firm lower and upper mass limits for KOI-89.01 and KOI-89.02 respectively. Additionally, the solution still points to near-circular, well-aligned orbits. We adopt this latter result assuming uniform priors on the mass ratios as the canonical one.

We note that the above solution is consistent with a previous dynamical analysis performed by Ahlers et al. (2015). Although their modeling of the light curve shape favored $e_2 \gtrsim 0.5$, they found that such solutions are not dynamically stable for 10^8 yr or longer. Instead, they found that the system can be long-term stable if $e_2 \lesssim 0.35$ and the orbits are co-planar. Here we presented a solution that satisfies this requirement and also explains the transit shapes and TTVs. We will show in Section 4 that this remains the case even if we take into account the possible effect of rapid stellar rotation on the transit shapes.

3.3.1. Dynamically Unstable Solutions Involving Large Eccentricities and Mutual Orbital Misalignment

The transit duration of KOI-89.02 (≈ 7 hr) is rather short given its orbital period of 208 days. In the analysis above, we find that this is well explained by a high impact parameter of the planet. On the other hand, the short transit duration alone is also compatible with a low impact parameter transit happening around the periastron of a highly eccentric orbit, as shown in Appendix A.1, and this was indeed the class of solutions favored by Ahlers et al. (2015). Such a solution might have been missed due to the too restrictive prior we imposed (i.e., $e_1 < 0.8$ and $e_2 < 0.45$). This motivated us to search for solutions where the eccentricity of KOI-89.02 is high. To cover the solution we did not explore, we repeated the photodynamical analysis choosing the prior $e_1 \sim \mathcal{U}(0, 0.9)$ and $e_2 \sim \mathcal{U}(0.45, 0.9)$. The priors on the other parameters were chosen to be the same, and log-uniform priors on the mass ratios were adopted.

From this analysis we found two solutions (i.e., two distinct posterior modes) implying $e_2 \sim 0.8$ and highly inclined ($\sim 120^\circ$) prograde and retrograde orbits. These solutions equally well match the observed light curves as the low-eccentricity solution, with the difference in the maximum log likelihood being less than unity.

However, these solutions would be short-lived: the same calculations as performed above show that 90 out of 100 randomly sampled systems become unstable within 10^7 inner orbits, and nine of the remaining 10 solutions exhibit $> 1\%$ variations in the inner semi-major axis at the end of the integration, hinting that the orbits would become unstable on longer timescales. Thus we conclude that these solutions are strongly disfavored in light of the \sim Gyr age of the host star.

3.4. Results: Three-planet Model

In Section 3.3, we showed that the two-planet model well explains the transit light curves of the two planets including TTVs. This is the simplest model given the current data, and there is no strong need to add another

planet. Nevertheless, here we explore three-planet models motivated by an unusually large mass ($\gtrsim 20 M_\oplus$) estimated for the inner KOI-89.01 given its size ($\approx 3 R_\oplus$), as we will discuss in more detail later (Section 5.2). This is a solid lower limit imposed by the large TTVs exhibited by KOI-89.02, whose orbit is not particularly close to that of KOI-89.01, nor to any low-order mean-motion resonances with it.

Here we fixed $\log_{10}(m_1/M_\star) = 0.77$ based on the Chen & Kipping (2017) mass-radius relation as a “reasonable” value for m_1 , and searched for solutions where the third planet (instead of KOI-89.01) may explain the TTVs of KOI-89.02. Here we assume that the three planets have mostly aligned orbits by fixing the longitudes of ascending nodes to be the same value and $\cos i_3$ to be zero, in the spirit of searching for solutions more typical of *Kepler* multi-planet systems.

Even under this simplification, given the sparse TTV data and the several new degrees of freedom introduced by the third planet, we expect that the solution will be complicated and multimodal. We therefore divided the prior range for P_3 into 24 equally-spaced log-intervals between $1.05 P_2$ and $4 P_2$, obtained posterior samples separately using the same **MultiNest** fitting, and combined them by weighing the evidence value for each interval. Mathematically, the normalized “partial” prior for the i th bin $p_i(P_3)$ (i.e., log-flat in the i th bin and zero otherwise) and the “full” normalized prior are related by $p(P_3) = \sum_i p_i(P_3)/N$ with N being the number of P_3 bins. Therefore,

$$\begin{aligned} p(\boldsymbol{\theta}, P_3 | \mathbf{d}) &= \frac{1}{N} \sum_i \frac{p(\mathbf{d} | \boldsymbol{\theta}, P_3)}{p(\mathbf{d})} p(\boldsymbol{\theta}) p_i(P_3) \\ &= \frac{1}{N} \sum_i \frac{p_i(\mathbf{d})}{p(\mathbf{d})} p_i(\boldsymbol{\theta}, P_3 | \mathbf{d}), \end{aligned} \quad (3)$$

where $\boldsymbol{\theta}$ is the set of parameters other than P_3 , $p_i(\boldsymbol{\theta}, P_3 | \mathbf{d})$ is the posterior conditioned on the partial prior $p(\boldsymbol{\theta}) p_i(P_3)$, and $p_i(\mathbf{d})$ is the corresponding evidence. Although the reliability of this “combined” posterior sample may be limited due to the limited accuracy of evidence evaluation, we believe that the sample is sufficient for our current purpose to capture the plausible range of three-planet solutions.

We find that the three-planet model can explain the data equally well as the two-planet model. The maximum likelihood value is slightly higher, but not high enough to favor the three-planet hypothesis over the two-planet one, considering the increased model complexity (e.g., in terms of the Bayesian information criterion). The constraints for the selected parameters are summarized in Table 3, although we note that m_3 and P_3 have multimodal marginal posteriors and the statis-

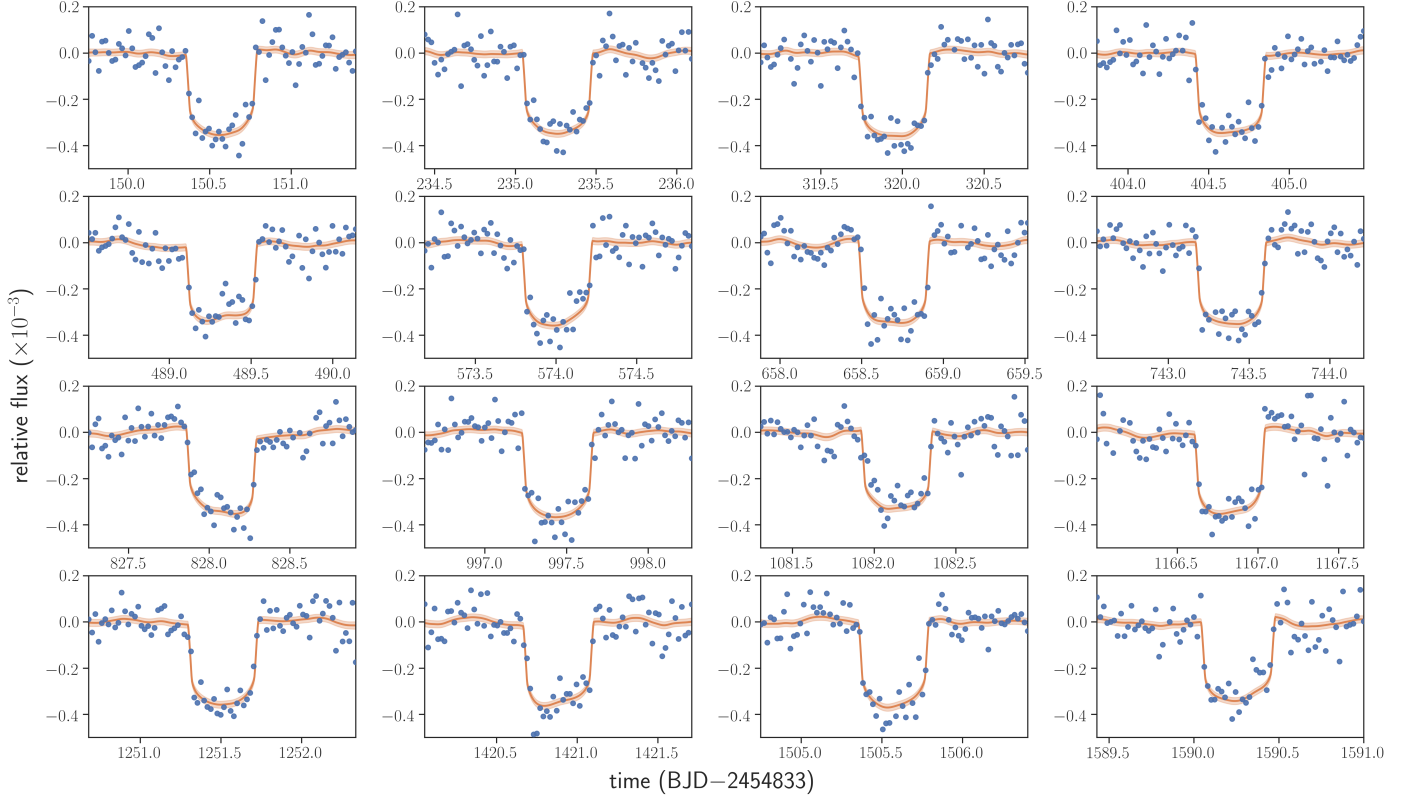


Figure 2. Transit light curves and posterior models for KOI-89.01. The blue filled circles show the observed flux values, and the orange lines show the maximum likelihood model with its standard deviation (shaded region).

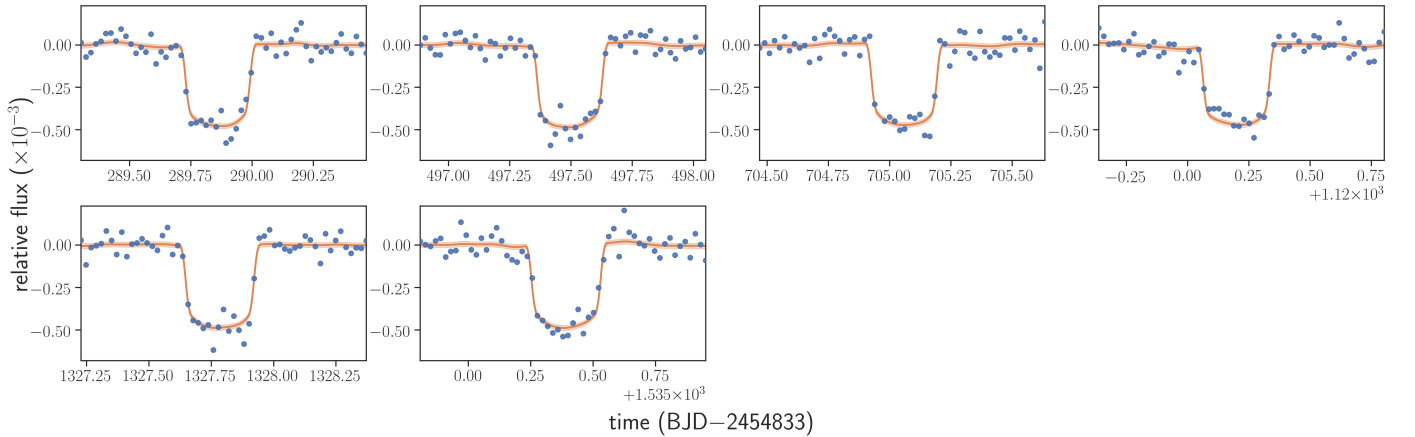


Figure 3. Transit light curves and posterior models for KOI-89.02. The blue filled circles show the observed flux values, and the orange lines show the maximum likelihood model with its standard deviation (shaded region).

tics here do not fully capture the complex nature of the solutions. We found significantly non-zero m_3 , which is consistent with our inference in the two-planet model that “normal” values of m_1 are insufficient to explain the strong TTVs of KOI-89.02. On the other hand, we found relatively well-constrained posteriors for the parameters of the inner two planets, including the mass of KOI-89.02 and eccentricities of both KOI-89.01 and

KOI-89.02. In this model two planets both have $10\text{--}20 M_{\oplus}$ (for $M_{\star} = 1.59 M_{\odot}$) and low eccentricities.

3.5. Conclusions

The findings from our photodynamical analysis are summarized as follows.

- Significant TTVs of KOI-89.02 suggest either an unusually large mass ($\gtrsim 20 M_{\oplus}$) for KOI-89.01

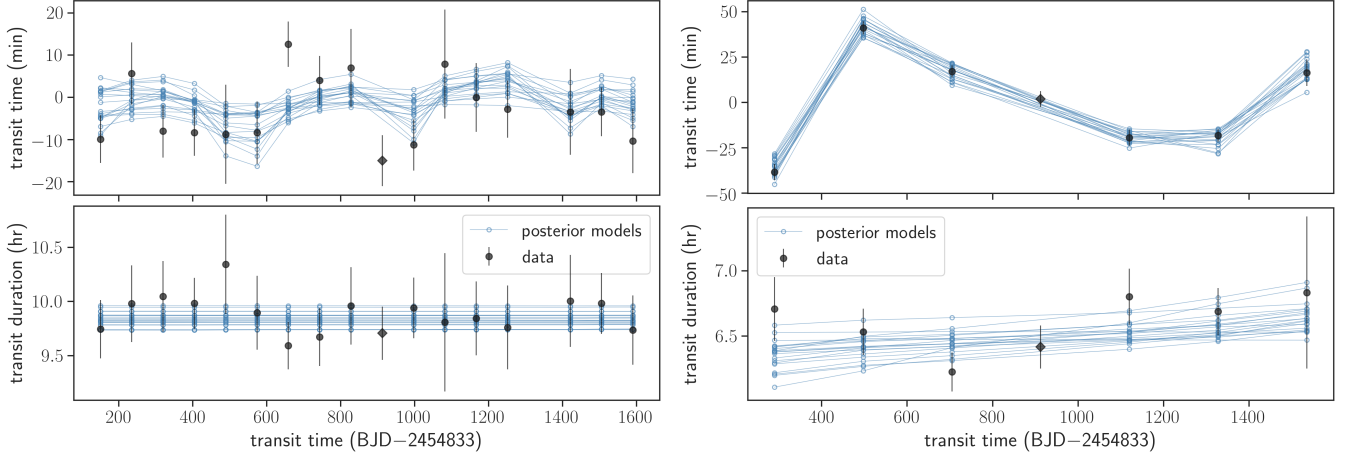


Figure 4. Transit times and durations measured by fitting individual transits (gray filled circles with error bars) and posterior models (blue open circles connected with lines). Note that these data are merely meant for illustration; we directly modeled the whole transit light curves (shown in Figure 2 and 3). *Left* — KOI-89.01, *Right* — KOI-89.02.

given its radius, or the presence of an undetected third planet.

- In both of the two-planet and three-planet models, the mass of KOI-89.02 is in the planetary range, and the orbits of KOI-89.01 and KOI-89.02 have low eccentricities.⁷ In the two-planet model, a low mutual inclination is also required by the data.

The above analysis also demonstrates an advantage of full photodynamical modeling over a two-step approach in which the TTVs and TDVs are derived first and then fitted with a dynamical model. The latter approach usually employs additional constraint on the mean impact parameter or the in-transit velocity (i.e., combination of the mean stellar density, eccentricity, and argument of periastron) derived from the transit shape, to solve the degeneracy between eccentricities and inclinations (e.g., Sanchis-Ojeda et al. 2012). This works well if the impact parameter is well constrained, but for KOI-89.02 the eccentricity and impact parameter are strongly degenerate as shown explicitly in Appendix A.1. In such a case, the result of the dynamical fit can depend sensitively on how those constraints from transit shapes are incorporated, and the issue could become more serious if the correlated noise in the light curve (which we modeled here) significantly affects those constraints. For example, if one adopts the mean (≈ 0.6) of the marginal posterior of the KOI-89.02’s transit impact parameter (Appendix A.1) and fits TTVs and TDVs, the modeling may erroneously favor high-eccentricity and mutually inclined

solutions as we explored in Section 3.3.1. For KOI-89, we were able to exclude these solutions based on stability argument in any case, but that may not always be possible. See also Dawson (2020) for an in-depth study of related issues.

4. ANALYSIS OF GRAVITY-DARKENED TRANSIT LIGHT CURVES

The star KOI-89 has a high projected rotation velocity $v \sin i_*$ of ≈ 80 km/s (Section 2). The rapid rotation results in the distorted stellar surface as well as associated inhomogeneity in the surface brightness distribution, the effect known as gravity darkening (von Zeipel 1924). The non-axisymmetric surface brightness distribution induced by the gravity darkening causes distortion of the transit light curve in such a way that depends on the stellar obliquity (Barnes 2009). Ahlers et al. (2015) argued that the transit of KOI-89.02 does exhibit gravity-darkening distortions and concluded that the star’s spin axis is tilted by $\approx 70^\circ$ from the orbital axes of the planets. The analysis used the stacked and binned transit light curves of the two planets, which involved a correction for the significant TTVs of KOI-89.02 and an inference of the unknown orbital eccentricity. We now revisit this analysis with our own TTV corrections and the associated prior knowledge on the eccentricities.

We analyze the stacked, long-cadence transit light curves of the two planets simultaneously. Given the significant TTVs of KOI-89.02, the stacking was performed by shifting each transit so that its central time becomes zero using the transit times derived by fitting each transit in Section 3.1. We did not correct for possible duration variations, which we did not detect significantly. Unlike in Ahlers et al. (2015), we chose *not* to bin the

⁷ The conclusion should remain unchanged even if the TTVs of KOI-89.02 is caused by a third planet in between KOI-89.01 and KOI-89.02, in which case there is even smaller room for solutions involving larger masses and eccentricities.

Table 2. Parameters of the KOI-89 System from Photodynamical Modeling.

	log-flat prior on mass ratios		flat prior on mass ratios		
	MAP & 68% HDI	95% HDI	MAP & 68% HDI	95% HDI	prior
<i>(host star)</i>					
mean density ρ_\star (g cm^{-3})	$0.50^{+0.06}_{-0.06}$	[0.40, 0.61]	$0.56^{+0.07}_{-0.07}$	[0.44, 0.68]	$\mathcal{N}(0.53, 0.06)$
limb-darkening coefficient $(u_1 + u_2)^2$	$0.20^{+0.08}_{-0.06}$	[0.09, 0.37]	$0.22^{+0.08}_{-0.07}$	[0.10, 0.40]	$\mathcal{U}(0, 1)$
limb-darkening coefficient $u_1/2(u_1 + u_2)$	$0.3^{+0.2}_{-0.2}$	[0.0, 0.7]	$0.3^{+0.2}_{-0.2}$	[0.0, 0.7]	$\mathcal{U}(0, 1)$
radius R_\star (R_\odot)	$1.63^{+0.07}_{-0.06}$	[1.52, 1.78]	$1.57^{+0.08}_{-0.06}$	[1.47, 1.73]	...
<i>(KOI-89.01)</i>					
mass ratio m_1/M_\star (M_\oplus/M_\odot)	$17.2^{+14.7}_{-4.9}$	[10.1, 52.4]	$35.7^{+64.2}_{-16.5}$	[16.4, 174.2]	$\mathcal{U}_{\log}(0.5, 100)$ / $\mathcal{U}(0, 200)$
orbital period P_1 (days)	$84.6873^{+0.0003}_{-0.0005}$	[84.6861, 84.6878]	$84.6866^{+0.0007}_{-0.0010}$	[84.6845, 84.6877]	$\mathcal{U}(84.58, 84.78)$
eccentricity e_1	$0.12^{+0.05}_{-0.03}$	[0.07, 0.21]	$0.042^{+0.046}_{-0.008}$	[0.031, 0.152]	$\mathcal{U}(0, 0.8)$ / $\mathcal{U}(0, 0.4)$
argument of periastron ω_1 (deg)	$57.0^{+7.9}_{-7.9}$	[42.2, 78.2]	$51.9^{+7.1}_{-11.3}$	[32.1, 66.1]	$\mathcal{U}(-180, 180)$
impact parameter b_1 (R_\star)	$0.1^{+0.1}_{-0.2}$	[-0.3, 0.3]	$-0.31^{+0.57}_{-0.06}$	[-0.47, 0.44]	$\mathcal{U}(-1, 1)$
longitude of ascending node Ω_1 (deg)	$-3.9^{+2.8}_{-5.2}$	[-16.1, 1.3]	$-1.2^{+1.1}_{-2.0}$	[-8.5, 0.7]	$\mathcal{U}(-180, 180)$ / $\mathcal{U}(-40, 40)$
time of inferior conjunction $t_{c,1}$	$150.574^{+0.002}_{-0.002}$	[150.571, 150.577]	$150.573^{+0.002}_{-0.002}$	[150.569, 150.577]	$\mathcal{U}(150.47, 150.67)$
radius ratio r_1/R_\star	$0.0175^{+0.0001}_{-0.0002}$	[0.0172, 0.0178]	$0.0175^{+0.0002}_{-0.0002}$	[0.0172, 0.0179]	$\mathcal{U}_{\log}(0.001, 0.1)$
mass m_1 (M_\oplus)	$27.9^{+23.3}_{-8.2}$	[15.7, 83.6]	$53.9^{+104.6}_{-23.8}$	[26.4, 278.6]	...
radius r_1 (R_\oplus)	$3.1^{+0.1}_{-0.1}$	[2.9, 3.4]	$3.0^{+0.2}_{-0.1}$	[2.8, 3.3]	...
mean density ρ_1 (g cm^{-3})	$4.3^{+4.9}_{-1.4}$	[2.3, 16.9]	$9.3^{+22.3}_{-4.6}$	[3.6, 57.2]	...
<i>(KOI-89.02)</i>					
mass ratio m_2/M_\star (M_\oplus/M_\odot)	$0.5004^{+1.6845}_{-0.0004}$	[0.5000, 5.7624]	$4.3^{+6.3}_{-3.5}$	[0.0, 18.3]	$\mathcal{U}_{\log}(0.5, 100)$ / $\mathcal{U}(0, 100)$
orbital period P_2 (days)	$207.620^{+0.008}_{-0.008}$	[207.605, 207.635]	$207.62^{+0.03}_{-0.01}$	[207.61, 207.69]	$\mathcal{U}_{\log}(207.38, 207.78)$
eccentricity e_2	$0.24^{+0.02}_{-0.06}$	[0.14, 0.29]	$0.11^{+0.05}_{-0.02}$	[0.09, 0.23]	$\mathcal{U}(0, 0.45)$
argument of periastron ω_2 (deg)	$12.8^{+4.5}_{-7.6}$	[-3.3, 21.4]	$14.9^{+3.2}_{-3.2}$	[7.3, 21.5]	$\mathcal{U}(-180, 180)$
impact parameter b_2 (R_\star)	$0.896^{+0.010}_{-0.008}$	[0.881, 0.914]	$0.890^{+0.011}_{-0.008}$	[0.874, 0.910]	$\mathcal{U}(0, 1)$
time of inferior conjunction $t_{c,2}$	$289.863^{+0.008}_{-0.005}$	[289.854, 289.881]	$289.87^{+0.03}_{-0.01}$	[289.86, 289.94]	$\mathcal{U}(289.66, 290.06)$
radius ratio r_2/R_\star	$0.0232^{+0.0004}_{-0.0003}$	[0.0226, 0.0239]	$0.0232^{+0.0004}_{-0.0003}$	[0.0225, 0.0239]	$\mathcal{U}_{\log}(0.001, 0.1)$
mass m_2 (M_\oplus)	$1.1^{+2.4}_{-0.3}$	[0.7, 9.2]	$6.0^{+10.8}_{-4.9}$	[0.0, 29.3]	...
radius r_2 (R_\oplus)	$4.1^{+0.2}_{-0.2}$	[3.8, 4.6]	$4.0^{+0.2}_{-0.2}$	[3.7, 4.4]	...
mean density ρ_2 (g cm^{-3})	$0.08^{+0.18}_{-0.03}$	[0.05, 0.77]	$0.4^{+1.1}_{-0.3}$	[0.0, 2.6]	...
mutual orbital inclination i_{12} (deg)	$3.8^{+4.1}_{-3.2}$	[0.3, 15.4]	$1.1^{+2.0}_{-0.7}$	[0.1, 7.9]	...
<i>(noise model)</i>					
$\ln \sigma_{\text{jit}}$	$-10.7^{+0.1}_{-0.2}$	[-11.1, -10.5]	$-10.7^{+0.1}_{-0.2}$	[-11.2, -10.4]	$\mathcal{U}(-13, -7)$
$\ln \alpha$	$-10.9^{+0.1}_{-0.1}$	[-11.2, -10.6]	$-10.9^{+0.1}_{-0.2}$	[-11.2, -10.6]	$\mathcal{U}(-13, -7)$
$\ln \rho$ (days)	$-2.6^{+0.3}_{-0.3}$	[-3.3, -2.1]	$-2.6^{+0.3}_{-0.4}$	[-3.4, -2.1]	$\mathcal{U}(-5, 1)$

NOTE—Values listed here report the maximum a posteriori (MAP) and 68%/95% highest density intervals (HDIs) of the marginal posteriors. Values without specified priors are the parameters that were not fitted directly, and are derived assuming a Gaussian distributed $M_* = 1.59 \pm 0.08 M_\odot$ when necessary. Longitude of the ascending node of KOI-89.02 is fixed to be zero, and arguments of the periastron are referred to the sky plane. Priors — $\mathcal{N}(\mu, \sigma)$ means the gaussian PDF centered on μ and width σ ; $\mathcal{U}(a, b)$ is the uniform PDF between a and b ; $\mathcal{U}_{\log}(a, b)$ is the log-uniform PDF between a and b . Dots indicate the parameters that were not directly sampled but were derived from the samples of the “fitted” parameters.

stacked light curves, because binning the long-cadence light curve may introduce additional shape distortion that is difficult to model and because the number of data points is small due to the long orbital period.

We modeled the gravity-darkened transit light curve as described in Masuda (2015), which is based on the formulation in Barnes (2009). The model involves the following parameters: mass, mean density, spin inclination measured from the line of sight i_* , projected rota-

Table 3. Masses and eccentricities from the three-planet photodynamical model.

	68% HDI	95% HDI	prior
m_1/M_\star (M_\oplus/M_\star)		5.89	fixed
m_2/M_\star (M_\oplus/M_\star)	[7.6, 14.7]	[5.6, 20.3]	$\mathcal{U}(0, 50)$
m_3/M_\star (M_\oplus/M_\star)	[43, 93]	[10, 94]	$\mathcal{U}(0, 100)$
e_1	[0.04, 0.12]	[0.03, 0.19]	$\mathcal{U}(0, 0.4)$
e_2	[0.00, 0.02]	[0.00, 0.06]	$\mathcal{U}(0, 0.4)$
e_3	[0.01, 0.05]	[0.00, 0.10]	$\mathcal{U}(0, 0.4)$
P_3 (days)	[478, 548]	[351, 739]	$\mathcal{U}_{\log}(218, 830)$
m_2 (M_\oplus)	[12.2, 23.6]	[8.8, 32.5]	...
m_3 (M_\oplus)	[65, 149]	[15, 152]	...

NOTE—Values listed here report the 68%/95% highest density intervals (HDIs) of the marginal posteriors derived using the method described in Section 3.4. Note that marginal posteriors for the mass and period of the third planet are multimodal and these parameters are poorly constrained. The physical masses are derived assuming a Gaussian distributed $M_\star = 1.59 \pm 0.08 M_\odot$ when necessary. Priors — $\mathcal{N}(\mu, \sigma)$ means the gaussian PDF centered on μ and width σ ; $\mathcal{U}(a, b)$ is the uniform PDF between a and b ; $\mathcal{U}_{\log}(a, b)$ is the log-uniform PDF between a and b . Dots indicate the parameters that were not directly sampled but were derived from the samples of the “fitted” parameters.

tion velocity, effective temperature at the pole, gravity-darkening exponent, limb-darkening coefficients for the star; and time of inferior conjunction, orbital period, eccentricity, argument of periastron, impact parameter, ratio of the planet radius to the stellar equatorial radius, and sky-projected obliquity λ for each of the planets. Here the stellar effective temperature was fixed to be 7540 K, and the limb-darkening coefficients were parameterized as in Kipping (2013) and treated as free parameters. Following Ahlers et al. (2020), the gravity darkening coefficient was chosen to be a deterministic function of the stellar oblateness (which in our model depends on the mass, mean density, projected rotation velocity, and inclination of the star) using the theoretical calculation in Espinosa Lara & Rieutord (2011); although the resulting values turned out to be fairly close to the standard value of 0.25 because the stellar oblateness was found to be $\mathcal{O}(1\%)$. We modeled the noise as a Gaussian process with the same Matérn-3/2 kernel and the white-noise term as in Equation 2, and marginalized over the noise parameters.

We fit the two transit light curves simultaneously, and obtained posterior samples of the model parameters using MultiNest (Feroz & Hobson 2008; Feroz et al. 2009, 2013) and its python interface PyMultiNest (Buchner

et al. 2014). We assumed separable, uniform or log-uniform priors for the model parameters (see Table 4) except for the following parameters. The prior for the mean density was chosen to be a Gaussian with mean 0.53 g cm^{-3} and dispersion 0.06 g cm^{-3} . For projected rotation velocity, we assumed a Gaussian with mean 85 km/s and dispersion 5 km/s. The choice is motivated by our derived value of $v \sin i_\star = 80 \pm 3 \text{ km/s}$ and the value of 90 km/s, which was adopted in Ahlers et al. (2015) based on the data from the *Kepler* Community Follow-up Observing Program. The prior on the eccentricities and arguments of periastron of the two planets was defined by the kernel density estimation of the joint posterior samples for the four parameters from the photodynamical modeling in Section 3. We did so both using the results from the two-planet model (Section 3.3) and the three-planet model (Section 3.4) and performed separate analyses.

Figure 5 shows the stacked light curves with the posterior samples for the model light curves. Table 4 summarizes the constraints from marginal posteriors. Figure 6 (top) shows a corner plot for the posterior samples of obliquity-related parameters, and Figure 6 (bottom) shows the marginal posterior distributions for the stellar obliquity relative to the orbits of the two planets. These results show that stellar obliquity is poorly constrained, both for the priors based on the two-planet and three-planet photodynamical models. This essentially means that the gravity darkening effect is not significantly detected in the light curves: in our solutions, gravity darkening causes $\mathcal{O}(1\%)$ change in the flux loss, which translates into $\sim 5 \times 10^{-6}$ in terms of the relative flux even for KOI-89.02 with the transit depth of 5×10^{-4} . This is much smaller than the observed noise level as seen, for example, in the bottom panels of Figure 5.

We also find that planet-to-star radius ratios and transit impact parameters from the gravity-darkened model agree with those from photodynamical modeling within $2\text{--}3\sigma$. This agreement is satisfactory given that the photodynamical model ignores $\mathcal{O}(1\%)$ distortion of the star: although we did not detect the gravity darkening effect on the surface brightness distribution significantly as discussed above, the model still incorporates geometric distortion (oblateness) of the star that does affect the estimated impact parameter and radius ratio. This systematic error is much smaller than the precision of the physical parameters of the system (including planet mass and radius) which is limited by the precision of the stellar mass determination. Thus the photodynamical modeling in Section 3 without taking into account gravity darkening is justified.

Table 4. Parameters from the Gravity-darkened Fit to the Stacked Transit Light Curves.

	prior from two-planet model		prior from three-planet model		
	MAP & 68% HDI	95% HDI	MAP & 68% HDI	95% HDI	prior
<i>(stellar parameters)</i>					
limb-darkening coefficient $(u_1 + u_2)^2$	$0.27^{+0.08}_{-0.08}$	[0.13, 0.43]	$0.26^{+0.08}_{-0.06}$	[0.14, 0.42]	$\mathcal{U}(0, 1)$
limb-darkening coefficient $u_1/2(u_1 + u_2)$	$0.3^{+0.1}_{-0.2}$	[0.0, 0.6]	$0.3^{+0.2}_{-0.1}$	[0.0, 0.5]	$\mathcal{U}(0, 1)$
mean density ρ_* (g cm^{-3})	$0.60^{+0.04}_{-0.04}$	[0.51, 0.67]	$0.59^{+0.04}_{-0.04}$	[0.52, 0.67]	$\mathcal{N}(0.53, 0.06)$
mass M_* (M_\odot)	$1.6^{+0.1}_{-0.1}$	[1.4, 1.8]	$1.59^{+0.09}_{-0.09}$	[1.39, 1.79]	$\mathcal{N}(1.59, 0.08)$
projected rotation velocity $v \sin i_*$ (km s^{-1})	$84.4^{+6.2}_{-6.0}$	[71.4, 96.4]	$83.9^{+5.7}_{-5.6}$	[72.3, 95.7]	$\mathcal{N}(85, 5)$
cosine of spin inclination $\cos i_*$	$-0.6^{+1.1}_{-0.1}$	[-0.8, 0.8]	$-0.6^{+0.5}_{-0.2}$	[-0.8, 0.7]	$\mathcal{U}(-1, 1)$
rotation period $P_{\text{rot}*}$ (days)	$0.8^{+0.1}_{-0.1}$	[0.5, 1.0]	$0.8^{+0.1}_{-0.1}$	[0.6, 1.0]	...
<i>(KOI-89.01)</i>					
time of inferior conjunction t_0 (days)	$0.000^{+0.001}_{-0.001}$	[-0.002, 0.003]	$0.0004^{+0.0010}_{-0.0009}$	[-0.0014, 0.0024]	$\mathcal{U}(-0.01, 0.01)$
planet-to-star radius ratio r/R_*	$0.0172^{+0.0001}_{-0.0002}$	[0.0170, 0.0176]	$0.0172^{+0.0001}_{-0.0002}$	[0.0169, 0.0175]	$\mathcal{U}_{\text{log}}(0.005, 0.05)$
eccentricity e	$0.05^{+0.03}_{-0.01}$	[0.03, 0.12]	$0.09^{+0.04}_{-0.03}$	[0.04, 0.19]	photodynamical
argument of periastron ω (deg)	$49.8^{+6.6}_{-8.8}$	[34.8, 63.2]	$154.9^{+13.6}_{-21.6}$	[88.0, 178.1]	modeling
impact parameter b (R_*)	$-0.14^{+0.31}_{-0.07}$	[-0.29, 0.29]	$-0.07^{+0.23}_{-0.06}$	[-0.24, 0.25]	$\mathcal{U}(-1, 1)$
sky-projected obliquity λ (deg)	$78.5^{+51.4}_{-172.6}$	[-151.3, 160.1]	$75.3^{+85.4}_{-56.9}$	[-136.7, 160.6]	$\mathcal{U}(-180, 180)$
<i>(KOI-89.02)</i>					
time of inferior conjunction t_0 (days)	$0.004^{+0.001}_{-0.005}$	[-0.005, 0.006]	$0.003^{+0.002}_{-0.004}$	[-0.005, 0.006]	$\mathcal{U}(-0.01, 0.01)$
planet-to-star radius ratio r/R_*	$0.0232^{+0.0003}_{-0.0004}$	[0.0223, 0.0238]	$0.0233^{+0.0003}_{-0.0004}$	[0.0225, 0.0239]	$\mathcal{U}_{\text{log}}(0.005, 0.05)$
eccentricity e	$0.12^{+0.03}_{-0.02}$	[0.09, 0.19]	$0.03^{+0.02}_{-0.02}$	[0.00, 0.07]	photodynamical
argument of periastron ω (deg)	$15.1^{+2.7}_{-2.6}$	[9.5, 20.4]	$99.5^{+69.5}_{-76.1}$	[-153.3, 179.9]	modeling
impact parameter b (R_*)	$0.869^{+0.007}_{-0.006}$	[0.858, 0.883]	$0.878^{+0.009}_{-0.009}$	[0.859, 0.894]	$\mathcal{U}(0, 1)$
sky-projected obliquity λ (deg)	$111.0^{+68.5}_{-171.8}$	[-163.7, 178.7]	$111.7^{+68.2}_{-131.9}$	[-155.2, 178.8]	$\mathcal{U}(-180, 180)$
<i>(noise parameters)</i>					
$\ln \sigma_{\text{jit}}$	$-10.51^{+0.07}_{-0.09}$	[-10.68, -10.36]	$-10.51^{+0.06}_{-0.09}$	[-10.68, -10.37]	$\mathcal{U}(-13, -7)$
$\ln \alpha$	$-12.3^{+0.5}_{-0.5}$	[-13.0, -11.5]	$-12.1^{+0.4}_{-0.5}$	[-13.0, -11.5]	$\mathcal{U}(-13, -7)$
$\ln \rho$ (days)	$-4.5^{+1.7}_{-0.5}$	[-5.0, -1.0]	$-4.2^{+1.2}_{-0.8}$	[-5.0, -1.6]	$\mathcal{U}(-5, 1)$

NOTE—Values listed here report the maximum a posteriori (MAP) and 68%/95% highest density intervals (HDIs) of the marginal posteriors. Priors — $\mathcal{N}(\mu, \sigma)$ means the gaussian PDF centered on μ and width σ ; $\mathcal{U}(a, b)$ is the uniform PDF between a and b ; $\mathcal{U}_{\text{log}}(a, b)$ is the log-uniform PDF between a and b . Dots indicate the parameters that were not directly sampled but were derived from the samples of the “fitted” parameters.

4.1. Possible Origins of the Difference with Previous Work

The inference of a large stellar obliquity in Ahlers et al. (2015) was largely based on an apparently V-shaped transit light curve for KOI-89.02 (their Figure 4), which was argued not to be well fit by a high impact parameter transit. This lead them to obtain a solution involving a rapidly rotating, nearly pole-on star. Indeed, the pole-to-equator flux contrast induced by strong gravity darkening can make transits V-shaped, and a pole-on configuration was also required to explain the observed $v \sin i_*$. The solution also involved a moderate impact parameter so that the planet can travel across the regions on the stellar surface with significantly different

surface brightness; this in turn led to a large eccentricity to explain the short observed transit duration.

The crux of the disagreement is therefore that we do not find the stacked transit light curve of KOI-89.02 to be V-shaped (Figure 5, bottom). The origin of the difference of the derived transit shapes is unclear, but possible explanations include incorrect TTV corrections and distortion due to the binning of the light curve. Our stacked light curve, as well as individual transits of KOI-89.02, are well modeled by a high-impact parameter orbit and obviate the need for a large stellar obliquity. In addition, we found that a large orbital eccentricity as required in the previous solution results in rapid orbital instability (as was also pointed out in Ahlers et al. 2015)

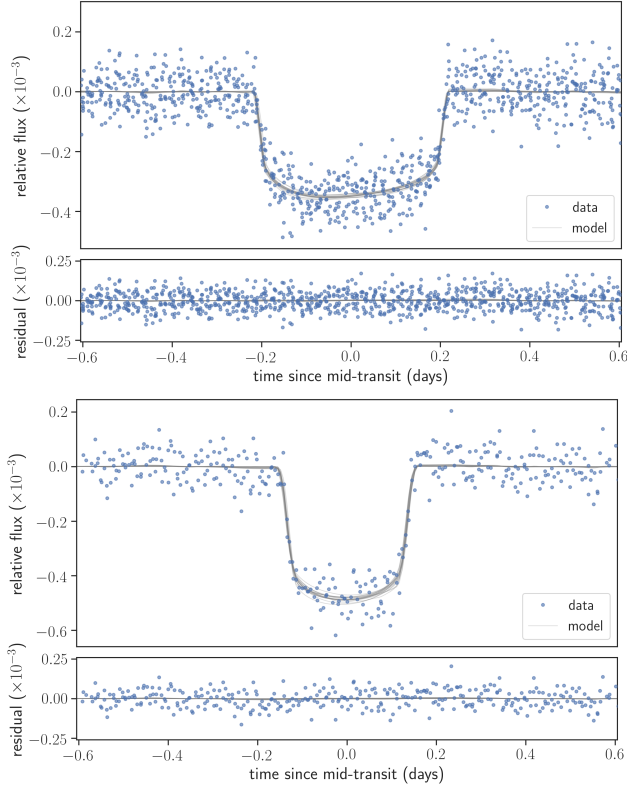


Figure 5. Modeling of the stacked transit light curves of KOI-89.01 (top) and KOI-89.02 (bottom). Blue dots show all the long-cadence data points. Gray solid lines are the gravity-darkened models computed for 20 parameter sets drawn from the posterior. The top panels show the flux data and model relative to one. The bottom panels show them after subtracting the maximum-likelihood transit model.

and is not favored from a dynamical point of view (see Section 3).

5. SUMMARY AND DISCUSSION

We performed a photodynamical analysis and transit shape modeling of the KOI-89/Kepler-462 system to constrain the masses and orbits of the two transiting planets (including the transiting KOI-89.02, which was previously classified as a candidate) and the spin of the host star. This is one of few multi-transiting systems confirmed around hot stars, for which Doppler masses are difficult to obtain. Our modeling of the transit light curves including mutual gravitational interactions indicate that the orbits of the two transiting planets have low eccentricities and a low mutual inclination. The modeling shows that the masses of both KOI-89.01/Kepler-462b and KOI-89.02 must be planetary, thus confirming KOI-89.02 to be a new planet (Kepler-462c). The large TTVs of KOI-89.02 suggest that either KOI-89.01/Kepler-462b is unusually massive given its size, or that there is a third planet that has

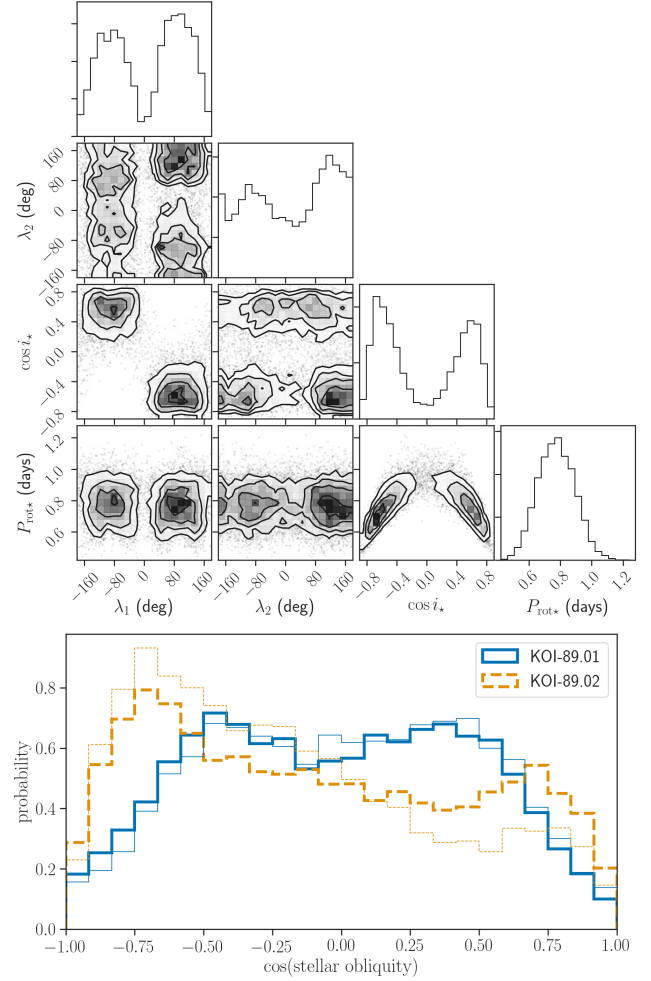


Figure 6. *Top* — Corner plot for the obliquity related parameters from the gravity-darkened fit. Here the prior from two-planet photodynamical model is adopted. *Bottom* — Marginal posterior distributions for the cosine of the stellar obliquity with respect to the orbits of KOI-89.01 (solid) and KOI-89.02 (dashed). Thicker lines are the results based on the eccentricity prior from the two-planet photodynamical model (Section 3.3) and thinner lines are based on the prior from the three-planet model (Section 3.4).

evaded transit detection but is significantly perturbing the orbit of KOI-89.02.

We also modeled the transit light curve of the two planets taking into account possible effects of gravity darkening of the rapidly rotating host star. We did not detect the signature of gravity darkening clearly, and concluded that stellar obliquity is not well constrained, as opposed to a previous claim. Below we discuss implications of those results.

5.1. Large Stellar Obliquity: Nature or Nurture?

We focused on the KOI-89 system because it is one of three multi-transiting systems with claimed significant

spin-orbit misalignments. Such systems might imply that the inner regions of planetary systems are occasionally misaligned with the stellar spin, for reasons unrelated to dynamical evolution of planetary orbits (e.g., misaligned disk). As discussed in Section 1, the large stellar obliquity in the other two systems, Kepler-56 and HD 3167, could plausibly be explained by dynamical evolution of the planetary orbits after formation. This left KOI-89 as the best known candidate for an obliquity excitation mechanism that does not alter planetary orbits.

Our reanalysis of the KOI-89 data shows that there is no evidence for a high stellar obliquity as previously claimed by Ahlers et al. (2015), although a high obliquity is not necessarily ruled out. We therefore conclude that there is currently no clear evidence for spin-orbit misalignments unrelated to dynamical orbital evolution from the available obliquity constraints on stars with multiple transiting planets.

Obliquity measurements for a larger number of individual multi-transiting systems will serve as a benchmark for untangling the origin of high obliquities. This is particularly important for hot stars like KOI-89, given the statistical evidence that high obliquities may be the norm among stars hotter than ≈ 6000 K, not only for those with hot Jupiters (Schlaufman 2010; Winn et al. 2010a; Albrecht et al. 2012) but for other *Kepler* stars with smaller and/or longer-period planets (Mazeh et al. 2015); although Winn et al. (2017) found otherwise and the reason of the apparent discrepancy remains unclear. Given that the majority of the samples in these works are stars with single transiting planets, which may be a part of multi-planetary systems with misaligned orbits (Zhu et al. 2018; He et al. 2019), these statistical results would be less sensitive to multi-transiting systems around hot stars. Obliquity constraints in multi-transiting systems would thus play a key role in uncovering the connection between the spin-orbit misalignment in generic *Kepler* systems around hot stars and dynamical excitation of planetary orbits.

5.2. Masses and Radii of the KOI-89 Planets

KOI-89.02 exhibits significant TTVs (Figure 4). The simplest explanation is that they are caused by KOI-89.01, and we showed that this model works well if KOI-89.01 is more massive than $\sim 20 M_{\oplus}$. The value is unusually high given its size ($\approx 3 R_{\oplus}$): such a planet is physically allowed, but we do not (yet) know of such planets (Figure 7, top). This motivated us to test the scenario in which the TTVs of KOI-89.02 are caused by another undetected planet. We found that this model also explains TTVs well for more “natural” masses for

the two transiting planets (Figure 7, bottom) — at the cost of increasing the model complexity to a level that is not justified by the data. It is in principle possible to quantify which model is favored from a Bayesian perspective, but the results would hardly be convincing given the lack of our current knowledge on the possible mass-radius relation, and on the plausible properties of the third planet conditioned on the properties of the star and two transiting planets.

Nevertheless, we feel that the two-planet solution with a massive KOI-89.01 is worth some discussion in light of recent observations that found planets with similar properties (i.e., prior knowledge that assigns more plausibility to a model involving a dense sub-Neptune). For example, Armstrong et al. (2020) reported the discovery of TOI-849b from the *Transiting Exoplanet Survey Satellite* (TESS) data. It is an ultra-short-period (0.765524 days) planet with a mass of $39.1^{+2.7}_{-2.6} M_{\oplus}$ and a radius of $3.44^{+0.16}_{-0.12} R_{\oplus}$. The mass and radius indicate that the gaseous envelope, if any, should be very thin and Armstrong et al. (2020) argued that KOI-849b may be the remnant core of a former giant planet. As shown in the top panel of Figure 7, the mass and radius of KOI-89.01 as inferred from the two-planet model is similar to TOI-849b, and imply that mass fraction of the gaseous envelope should be a few percent or less. If the two-planet model is correct, KOI-89.01, with an orbital period of 85 days, would suggest that such a massive core without a thick envelope can form further away from the star where the effect of photoevaporation is less significant. This poses a theoretical challenge similar to the one posed by super Earths: why would such a planet not grow into a gas giant? This property is even more puzzling in the presence of the outer less massive KOI-89.02 with a thicker atmosphere (as simply implied by its larger radius), whose core would have had a longer formation timescale than the inner KOI-89.01, all else being equal. Such a large contrast in the mean densities has been observed in the Kepler-36 system (Carter et al. 2012) and has been explained by photoevaporation (e.g., Lopez & Fortney 2013), but the planets of KOI-89 are much further away from the star where this explanation would not work. This might then suggest that accretion onto planetary cores significantly depends on the surrounding environment.

Another implication of the two-planet solution is that such dense, (sub-)Neptune-sized planets may be abundant on orbits wider than have been probed with Doppler surveys to date. If so, Doppler follow-up observations of relatively long-period transiting Neptune-sized planets orbiting bright stars from *K2* or *TESS* would reveal more such planets. HD 95338 b (Díaz et al.

2020), a planet with $42.4^{+2.2}_{-2.1} M_{\oplus}$ and $3.89^{+0.19}_{-0.20} R_{\oplus}$ (Figure 7, top) on a 55-day period orbit around a bright K dwarf observed by *TESS*, may be such an example.

ACKNOWLEDGMENTS

The authors thank the referee, Jason Barnes, for his constructive comments which helped to improve the clarity of this paper. KM gratefully acknowledges the support by the W.M. Keck Foundation Fund at the Institute for Advanced Study, where a part of this work was performed. Support for DT was provided by NASA through the NASA Hubble Fellowship grant HST-HF2-51423.001-A awarded by the Space Telescope Science Institute, which is operated by the Association of Universities for Research in Astronomy, Inc., for NASA, under contract NAS5-26555. Simulations in this paper made use of the **REBOUND** code which is freely available at <http://github.com/hannorein/rebound>.

APPENDIX

A. LIGHT-CURVE ANALYSIS

A.1. Modeling of the Stacked Transit Light Curves with a Normal Transit Model

Here we present modeling of the stacked transit light curves as processed in Section 3.1 using the model for a quadratically limb-darkened star (Luger et al. 2019). We do not include the effect of gravity darkening, and fit for orbital eccentricities without incorporating the prior knowledge from photodynamical modeling. The analysis here is meant to illustrate the possible range of solutions prior to the modeling of dynamical interactions.

The modeling was performed using **exoplanet** (Foreman-Mackey et al. 2020) and its dependencies (Agol et al. 2019; Astropy Collaboration et al. 2013, 2018; Kipping 2013; Luger et al. 2019; Salvatier et al. 2016; Theano Development Team 2016). The posterior samples were obtained for the parameters listed in Table 5 using the prior in the rightmost column. The noise was modeled using the Gaussian process kernel in Equation 2, and the light curve of each planet was modeled individually. Table 5 summarizes the resulting HDIs for marginal posteriors, and Figure 8 shows corner plots (Foreman-Mackey 2016) for the radius ratio, impact parameter, and eccentricity.

For the radius ratios, we find good agreement with the results of photodynamical modeling in Section 3 using unstacked light curves, and gravity-darkened modeling of stacked light curves in Section 4 that adopted a gravity-darkened model. On the other hand, eccentricity and impact parameter are poorly constrained based only on the shapes of the stacked light curves and the prior on the mean stellar density, and these parameters

exhibit strong correlations as shown in Figure 8. We note that the marginal posterior for the eccentricity of KOI-89.02 is peaked at a high value, but lower values are also allowed. The former is the solutions found by Ahlers et al. (2015), and we found that the latter should be the case from photodynamical modeling in Section 3. Such a posterior is found because the duration of KOI-89.02 is relatively short for the given orbital period and prior on the mean density (\sim stellar radius), and because the durations of ingress/egress are not well constrained by the data: here the short duration can be explained either by a large, finely tuned b and a low e , or a high e and a wider range of b . The latter solution has a larger volume in the parameter space and produces a peak in the marginal posterior for e . This example illustrates the importance of carefully interpreting the short-duration transits.

A.2. Central Times and Durations of Individual Transits

We also fitted individual transits separately using **exoplanet** with the same noise model. This time we fixed $e = 0$ and set log-uniform prior on the mean stellar density, because we are interested only in empirically constraining mid-transit times and transit durations calculated as $T = (R_{\star}P/\pi a)\sqrt{1 - b^2}$ (Winn 2010), so that TTVs and TDVs can be visualized and compared to the results of the full photodynamical modeling. Here we also modeled the overlapping transit of the two planets around $\text{BJD}_{\text{TDB}} = 2454833 + 912.7$, so that the values can be used to test predictions based on the other transits used for the photodynamical modeling. The resulting transit times and durations (medians and symmetric 68% intervals of the marginal posteriors) are shown in

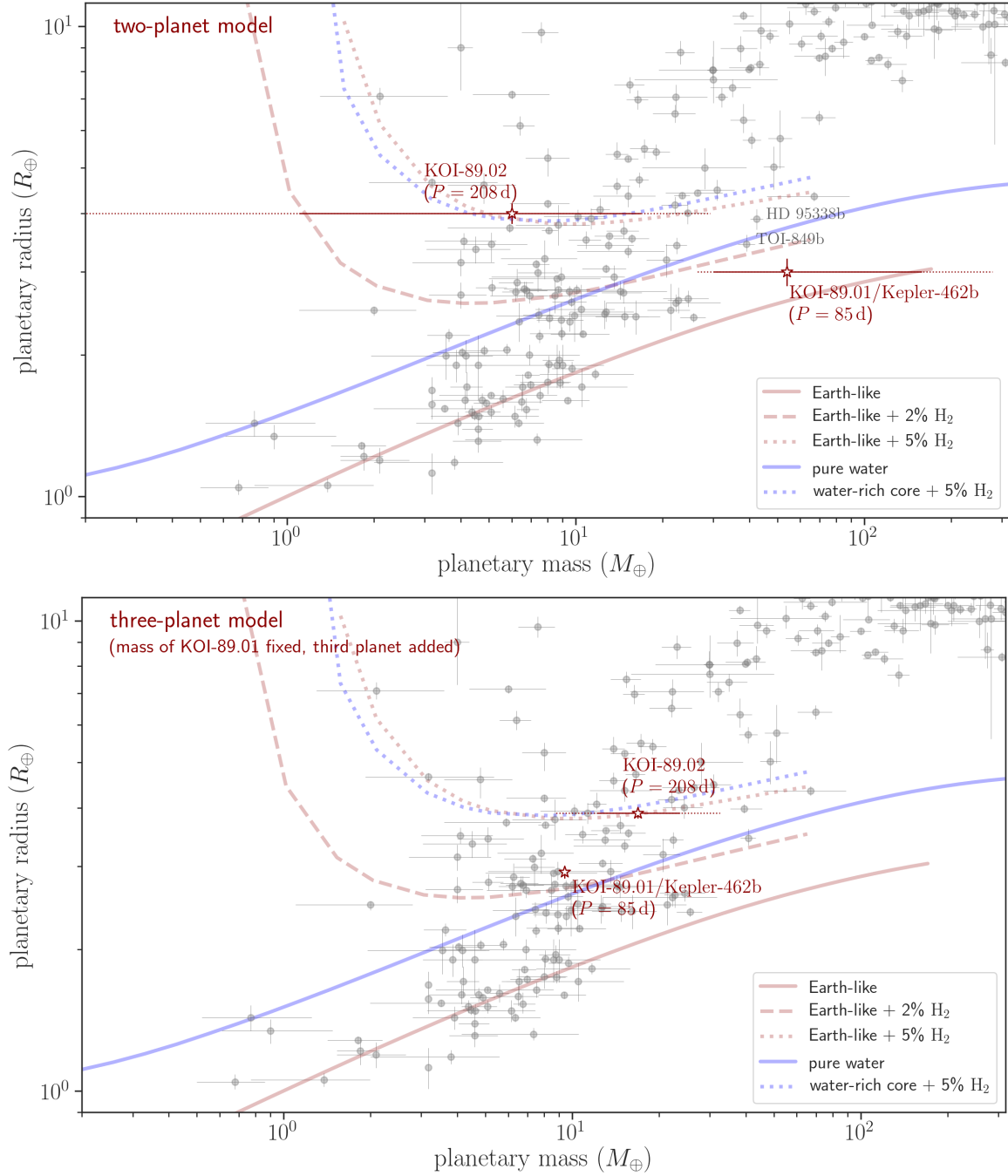


Figure 7. Radius-mass diagram of planets smaller and less massive than Jupiter (gray circles with error bars). The selection criteria are similar to the ones in Figure 1, except that planets with masses from Hadden & Lithwick (2014) and Xie (2014) are removed because those masses are derived using the analytic TTV formula (Lithwick et al. 2012) without taking into account the dependence on free eccentricities. Star symbols with error bars show the estimated parameters of the locations of the KOI-89 planets, for the two-planet (top) and three-planet (bottom) photodynamical models (see Section 3 for details). The locations of the symbols show the maximum a posteriori values, and solid (dotted) error bars correspond to 68% (95%) highest density intervals of the marginal posteriors. Solid, dashed, and dotted curves show theoretical radius-mass relations from Zeng et al. (2019).

Figure 4. We emphasize again that these transit times and durations were not used for any modeling, but are compared with the output of the photodynamical modeling in Section 3 only for an illustrative purpose.

B. CONSTRAINTS ON MUTUAL ORBITAL INCLINATIONS IN THE TWO-PLANET MODEL WITH LOW ECCENTRICITIES

In Section 3.3, we argued that two-body models with low-eccentricity, highly inclined orbits are disfavored by the lack of TDVs. Here we show how the goodness of fit depends on the mutual orbital inclination, which in our case is essentially the same as the orbital misalignment in the sky plane, Ω_1 . We repeated the posterior sampling with uniform priors on the mass ratios as in Section 3.3, separately for 18 equally-spaced intervals of Ω_1 . Figure 9 shows the resulting posterior samples with the log-

likelihood values (multiplied by -2 so that they analogize with chi-squared), where the vertical lines indicate the boundaries of the Ω_1 intervals. As we argued in the main text, the best solution is around $\Omega_1 = 0^\circ$. Those solutions with intermediate $|\Omega_1| \sim 30^\circ$ give a bad fit because the durations of KOI-89.02 drift too much (Figure 10, top). There exist local minima around $|\Omega_1| \sim 90^\circ$ because the duration variations due to nodal precession are minimized for nearly orthogonal orbits. However, in this case KOI-89.02 receives kicks perpendicular to its orbit and its durations still fluctuate more than allowed by the data (Figure 10, bottom). We note that better solutions than shown in Figure 9 exist for most values of $\Omega_1 \neq 0$ if larger values of eccentricity are considered for KOI-89.02. However, those solutions are disfavored from the stability point of view, as discussed in Section 3.3.1.

REFERENCES

- Agol, E., Luger, R., & Foreman-Mackey, D. 2019, arXiv e-prints, 1908.03222
- Ahlers, J. P., Barnes, J. W., & Barnes, R. 2015, *ApJ*, 814, 67
- Ahlers, J. P., Kruse, E., Colón, K. D., et al. 2020, *ApJ*, 888, 63
- Albrecht, S., Winn, J. N., Marcy, G. W., et al. 2013, *ApJ*, 771, 11
- Albrecht, S., Winn, J. N., Johnson, J. A., et al. 2012, *ApJ*, 757, 18
- Armstrong, D. J., Lopez, T. A., Adibekyan, V., et al. 2020, *Nature*, 583, 39
- Astropy Collaboration, Robitaille, T. P., Tollerud, E. J., et al. 2013, *aap*, 558, A33
- Astropy Collaboration, Price-Whelan, A. M., SipH ocz, B. M., et al. 2018, *aj*, 156, 123
- Bailer-Jones, C. A. L., Rybizki, J., Foesneau, M., Mantelet, G., & Andrae, R. 2018, *AJ*, 156, 58
- Barnes, J. W. 2009, *ApJ*, 705, 683
- Bate, M. R., Lodato, G., & Pringle, J. E. 2010, *MNRAS*, 401, 1505
- Batygin, K. 2012, *Nature*, 491, 418
- Batygin, K., & Adams, F. C. 2013, *ApJ*, 778, 169
- Berger, T. A., Huber, D., Gaidos, E., & van Saders, J. L. 2018, *ApJ*, 866, 99
- Bourrier, V., Lovis, C., Beust, H., et al. 2018, *Nature*, 553, 477
- Boyajian, T. S., von Braun, K., van Belle, G., et al. 2013, *ApJ*, 771, 40
- Brahm, R., Jordán, A., & Espinoza, N. 2017a, *PASP*, 129, 034002
- Brahm, R., Jordán, A., Hartman, J., & Bakos, G. 2017b, *MNRAS*, 467, 971
- Buchner, J., Georgakakis, A., Nandra, K., et al. 2014, *A&A*, 564, A125
- Carter, J. A., Agol, E., Chaplin, W. J., et al. 2012, *Science*, 337, 556
- Chaplin, W. J., Sanchis-Ojeda, R., Campante, T. L., et al. 2013, *ApJ*, 766, 101
- Chatterjee, S., Ford, E. B., Matsumura, S., & Rasio, F. A. 2008, *ApJ*, 686, 580
- Chen, J., & Kipping, D. 2017, *ApJ*, 834, 17
- Choi, J., Dotter, A., Conroy, C., et al. 2016, *ApJ*, 823, 102
- Cui, X.-Q., Zhao, Y.-H., Chu, Y.-Q., et al. 2012, *Research in Astronomy and Astrophysics*, 12, 1197
- Dai, F., Masuda, K., & Winn, J. N. 2018, *ApJL*, 864, L38
- Dalal, S., Hébrard, G., Lecavelier des Étangs, A., et al. 2019, *A&A*, 631, A28
- Damasso, M., Sozzetti, A., Lovis, C., et al. 2020, arXiv e-prints, arXiv:2007.06410
- Davies, C. L. 2019, *MNRAS*, 484, 1926
- Dawson, R. I. 2020, *AJ*, 159, 223
- De Rosa, R. J., Dawson, R., & Nielsen, E. L. 2020, arXiv e-prints, arXiv:2007.08549
- Deck, K. M., Agol, E., Holman, M. J., & Nesvorný, D. 2014, *ApJ*, 787, 132
- Díaz, M. R., Jenkins, J. S., Feng, F., et al. 2020, *MNRAS*, 496, 4330
- Dotter, A. 2016, *ApJS*, 222, 8
- Espinosa Lara, F., & Rieutord, M. 2011, *A&A*, 533, A43
- Fabrycky, D., & Tremaine, S. 2007, *ApJ*, 669, 1298
- Feroz, F., & Hobson, M. P. 2008, *MNRAS*, 384, 449

Table 5. Parameters from Phase-folded Transit Light Curves.

	KOI-89.01		KOI-89.02		prior
	68% HDI	95% HDI	68% HDI	95% HDI	
time of inferior conjunction t_0 (days)	[−0.001, 0.001]	[−0.002, 0.003]	[−0.001, 0.002]	[−0.002, 0.003]	$\mathcal{N}(0, 0.05)$
radius ratio r/R_*	[0.0171, 0.0178]	[0.0169, 0.0183]	[0.0205, 0.0227]	[0.0201, 0.0240]	$\mathcal{U}_{\log}(0.001, 0.05)$
impact parameter b	[0.09, 0.51]	[0.00, 0.66]	[0.46, 0.92]	[0.07, 0.92]	$\mathcal{U}(0, 1 + r/R_*)$
eccentricity e	[0.00, 0.28]	[0.00, 0.61]	[0.40, 0.86]	[0.07, 0.89]	$\mathcal{U}(0, 0.9)$
argument of periastron ω (deg)	[−35, 180]	[−180, 169]	[8, 151]	[−158, 180]	$\mathcal{U}(−180, 180)$
mean stellar density ρ_* (g cm^{-3})	[0.47, 0.59]	[0.42, 0.65]	[0.47, 0.59]	[0.43, 0.66]	$\mathcal{N}(0.53, 0.06)$
limb-darkening coefficients $(u_1 + u_2)^2$	[0.23, 0.54]	[0.13, 0.80]	[0.06, 0.30]	[0.00, 0.59]	$\mathcal{U}(0, 1)$
limb-darkening coefficients $u_1/2(u_1 + u_2)$	[0.00, 0.20]	[0.00, 0.48]	[0.00, 0.44]	[0.00, 0.87]	$\mathcal{U}(0, 1)$
mean flux (10^{-5})	[−0.3, 0.4]	[−1.1, 1.2]	[−0.5, 0.6]	[−1.5, 1.5]	$\mathcal{N}(0, 10^3)$
$\ln \sigma_{\text{jit}}$	[−10.5, −10.3]	[−10.6, −10.3]	[−12.4, −10.9]	[−13.0, −10.7]	$\mathcal{U}(−13, −7)$
$\ln \alpha$	[−12.6, −11.4]	[−13.0, −10.9]	[−12.0, −10.7]	[−13.0, −10.6]	$\mathcal{U}(−13, −7)$
$\ln \rho$ (days)	[−4.1, −0.8]	[−5.0, 0.4]	[−5.0, −2.1]	[−5.0, 0.4]	$\mathcal{U}(−5, 1)$

NOTE—Values listed here are the 68%/95% highest density intervals (HDIs) of the marginal posteriors. Priors — $\mathcal{N}(\mu, \sigma)$ means the gaussian PDF centered on μ and width σ ; $\mathcal{U}(a, b)$ is the uniform PDF between a and b ; $\mathcal{U}_{\log}(a, b)$ is the log-uniform PDF between a and b .

Feroz, F., Hobson, M. P., & Bridges, M. 2009, MNRAS, 398, 1601

Feroz, F., Hobson, M. P., Cameron, E., & Pettitt, A. N. 2013, ArXiv e-prints, arXiv:1306.2144

Fielding, D. B., McKee, C. F., Socrates, A., Cunningham, A. J., & Klein, R. I. 2015, MNRAS, 450, 3306

Foreman-Mackey, D. 2016, The Journal of Open Source Software, 24, doi:10.21105/joss.00024

Foreman-Mackey, D., Agol, E., Angus, R., & Ambikasaran, S. 2017, ArXiv

Foreman-Mackey, D., Luger, R., Czekala, I., et al. 2020, exoplanet-dev/exoplanet v0.3.2, , , doi:10.5281/zenodo.1998447

Frasca, A., Molenda-Żakowicz, J., De Cat, P., et al. 2016, A&A, 594, A39

Fulton, B. J., & Petigura, E. A. 2018, AJ, 156, 264

Gaia Collaboration, Brown, A. G. A., Vallenari, A., et al. 2018, A&A, 616, A1

Gratia, P., & Fabrycky, D. 2017, MNRAS, 464, 1709

Greaves, J. S., Kennedy, G. M., Thureau, N., et al. 2014, MNRAS, 438, L31

Green, G. M., Schlafly, E. F., Finkbeiner, D., et al. 2018, MNRAS, 478, 651

Hadden, S., & Lithwick, Y. 2014, ApJ, 787, 80

He, M. Y., Ford, E. B., & Ragozzine, D. 2019, MNRAS, 490, 4575

Hébrard, G., Bouchy, F., Pont, F., et al. 2008, A&A, 488, 763

Hirano, T., Narita, N., Sato, B., et al. 2012, ApJL, 759, L36

Hirano, T., Gaidos, E., Winn, J. N., et al. 2020, ApJL, 890, L27

Holman, M., Touma, J., & Tremaine, S. 1997, Nature, 386, 254

Huang, C. X., Petrovich, C., & Deibert, E. 2017, AJ, 153, 210

Huber, D., Carter, J. A., Barbieri, M., et al. 2013, Science, 342, 331

Husser, T. O., Wende-von Berg, S., Dreizler, S., et al. 2013, A&A, 553, A6

Jurić, M., & Tremaine, S. 2008, ApJ, 686, 603

Kamiaka, S., Benomar, O., Suto, Y., et al. 2019, AJ, 157, 137

Kipping, D. M. 2013, MNRAS, 435, 2152

Kreidberg, L. 2015, PASP, 127, 1161

Kunovac Hodžić, V., Triaud, A. H. M. J., Cegla, H. M., Chaplin, W. J., & Davies, G. R. 2020, arXiv e-prints, arXiv:2007.11564

Lai, D. 2014, MNRAS, 440, 3532

Lai, D., & Pu, B. 2017, AJ, 153, 42

Li, G., Naoz, S., Valsecchi, F., Johnson, J. A., & Rasio, F. A. 2014, ApJ, 794, 131

Lithwick, Y., Xie, J., & Wu, Y. 2012, ApJ, 761, 122

Lopez, E. D., & Fortney, J. J. 2013, ApJ, 776, 2

Luger, R., Agol, E., Foreman-Mackey, D., et al. 2019, aj, 157, 64

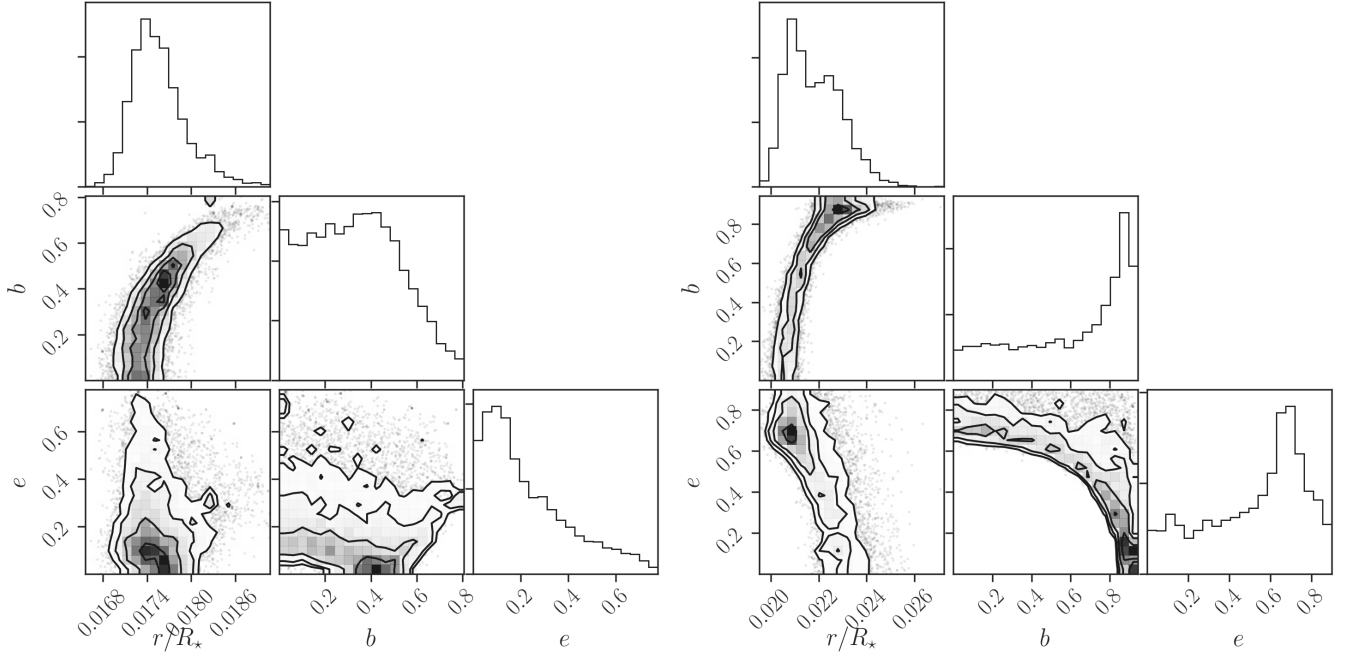


Figure 8. Corner plots for the posterior samples of radius ratios, impact parameters, and eccentricities of KOI-89.01 (left) KOI-89.02 (right).

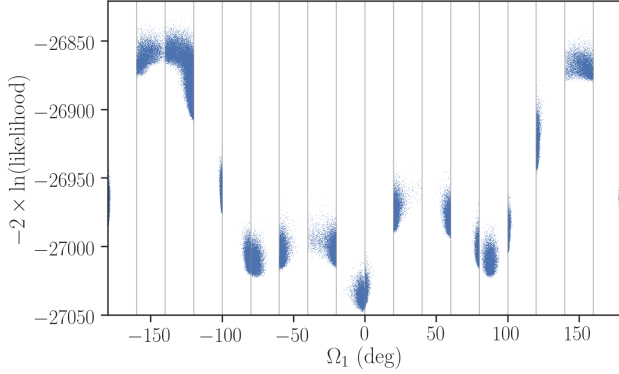


Figure 9. Dependence of the likelihood on Ω_1 in the two-planet model with low-eccentricity orbits.

- Luo, A.-L., Zhao, Y.-H., Zhao, G., et al. 2015, *Research in Astronomy and Astrophysics*, 15, 1095
- Mandel, K., & Agol, E. 2002, *ApJL*, 580, L171
- Mann, A. W., Johnson, M. C., Vanderburg, A., et al. 2020, arXiv e-prints, arXiv:2005.00047
- Masuda, K. 2015, *ApJ*, 805, 28
- Masuda, K., Winn, J. N., & Kawahara, H. 2020, *AJ*, 159, 38
- Mathur, S., Huber, D., Batalha, N. M., et al. 2017, *ApJS*, 229, 30
- Mazeh, T., Krymolowski, Y., & Rosenfeld, G. 1997, *ApJL*, 477, L103
- Mazeh, T., Perets, H. B., McQuillan, A., & Goldstein, E. S. 2015, *ApJ*, 801, 3
- Mills, S. M., & Fabrycky, D. C. 2017, *AJ*, 153, 45

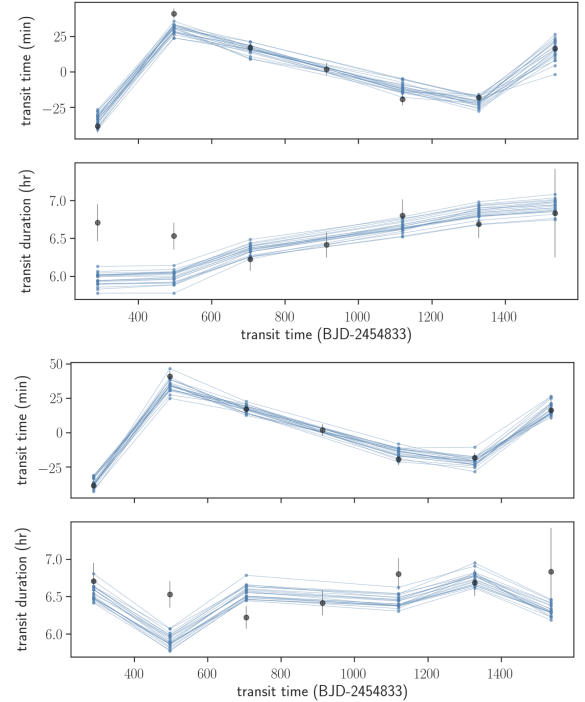


Figure 10. TTV and TDV solutions of KOI-89.02 for the fits restricted to $\Omega_1 = [-40^\circ, -20^\circ]$ (top) and $\Omega_1 = [-100^\circ, -80^\circ]$ (bottom).

- Miralda-Escudé, J. 2002, *ApJ*, 564, 1019
- Morton, T. D. 2015, isochrones: Stellar model grid package, *Astrophysics Source Code Library*, , ascl:1503.010

- Naoz, S., Farr, W. M., Lithwick, Y., Rasio, F. A., & Teyssandier, J. 2011, *Nature*, 473, 187
- Otor, O. J., Montet, B. T., Johnson, J. A., et al. 2016, *AJ*, 152, 165
- Paxton, B., Bildsten, L., Dotter, A., et al. 2011, *ApJS*, 192, 3
- Paxton, B., Cantiello, M., Arras, P., et al. 2013, *ApJS*, 208, 4
- Paxton, B., Marchant, P., Schwab, J., et al. 2015, *ApJS*, 220, 15
- Petigura, E. A., Marcy, G. W., & Howard, A. W. 2013, *ApJ*, 770, 69
- Rasio, F. A., & Ford, E. B. 1996, *Science*, 274, 954
- Rein, H., & Liu, S. F. 2012, *A&A*, 537, A128
- Rein, H., & Spiegel, D. S. 2015, *MNRAS*, 446, 1424
- Rogers, T. M., Lin, D. N. C., & Lau, H. H. B. 2012, *ApJL*, 758, L6
- Rowe, J. F., Bryson, S. T., Marcy, G. W., et al. 2014, *ApJ*, 784, 45
- Salvatier, J., Wiecki, T. V., & Fonnesbeck, C. 2016, *PeerJ Computer Science*, 2, e55
- Sanchis-Ojeda, R., Fabrycky, D. C., Winn, J. N., et al. 2012, *Nature*, 487, 449
- Sanchis-Ojeda, R., Winn, J. N., Dai, F., et al. 2015, *ApJL*, 812, L11
- Schlaufman, K. C. 2010, *ApJ*, 719, 602
- Skrutskie, M. F., Cutri, R. M., Stiening, R., et al. 2006, *AJ*, 131, 1163
- Southworth, J. 2011, *MNRAS*, 417, 2166
- Spalding, C., & Batygin, K. 2014, *ApJ*, 790, 42
- . 2015, *ApJ*, 811, 82
- Stassun, K. G., Oelkers, R. J., Paegert, M., et al. 2019, *AJ*, 158, 138
- Takaishi, D., Tsukamoto, Y., & Suto, Y. 2020, *MNRAS*, 492, 5641
- Theano Development Team. 2016, arXiv e-prints, abs/1605.02688
- von Zeipel, H. 1924, *MNRAS*, 84, 665
- Wang, S., Addison, B., Fischer, D. A., et al. 2018, *AJ*, 155, 70
- Watson, C. A., Littlefair, S. P., Diamond, C., et al. 2011, *MNRAS*, 413, L71
- Weidenschilling, S. J., & Marzari, F. 1996, *Nature*, 384, 619
- Winn, J. N. 2010, ArXiv e-prints, arXiv:1001.2010
- Winn, J. N., Fabrycky, D., Albrecht, S., & Johnson, J. A. 2010a, *ApJL*, 718, L145
- Winn, J. N., Johnson, J. A., Howard, A. W., et al. 2010b, *ApJL*, 723, L223
- Winn, J. N., Petigura, E. A., Morton, T. D., et al. 2017, *AJ*, 154, 270
- Xie, J.-W. 2014, *ApJS*, 210, 25
- Xuan, J. W., & Wyatt, M. C. 2020, *MNRAS*, arXiv:2007.01871
- Zanazzi, J. J., & Lai, D. 2018, *MNRAS*, 478, 835
- Zeng, L., Jacobsen, S. B., Sasselov, D. D., et al. 2019, *Proceedings of the National Academy of Science*, 116, 9723
- Zhou, G., Rodriguez, J. E., Vanderburg, A., et al. 2018, *AJ*, 156, 93
- Zhu, W., Petrovich, C., Wu, Y., Dong, S., & Xie, J. 2018, *ApJ*, 860, 101